A Path-Following Method Based on Plastic Dissipation Control

Boštjan Brank, Andjelka Stanić and Adnan Ibrahimbegovic

Abstract A path-following method that is based on controlling incremental plastic dissipation is presented. It can be applied for analysis of an elasto-plastic solid or structure. It can be also applied for complete failure computation of a solid or structure that is performed by using a material failure model. In this work, we applied it for computations with the embedded-discontinuity finite elements that use rigid-plastic cohesive laws with softening to model material failure process. The most important part of the path-following method is the constraint function. Several constraint functions are derived and proposed for geometrically nonlinear small strain elasto-plasticity with linear isotropic hardening. The constraint functions are also derived for the embedded-discontinuity finite elements. In particular, they are derived for 2-d solid (and frame) embedded-discontinuity finite elements that describe cohesive stresses (or forces and moments) in the discontinuity curve (or point) by rigid-plasticity with softening. Numerical examples are presented in order to illustrate performance of the discussed path-following method.

1 Introduction

The most used path-following method in the nonlinear finite element analysis of solids and structures is probably the Crisfield's cylindrical arc-length method, see e.g. [1]. It can be successfully used for solving geometrically linear problems as well as many types of geometrically and materially nonlinear problems. However,

B. Brank (✉) · A. Stanić
Faculty of Civil and Geodetic Engineering, University of Ljubljana,
Jamova cesta 2, 1000 Ljubljana, Slovenia
e-mail: bbrank@fgg.uni-lj.si

A. Ibrahimbegovic
Laboratory Roberval, University of Technology of Compiègne,
Compiègne, France

A. Ibrahimbegovic (ed.), *Computational Methods for Solids and Fluids*,
Computational Methods in Applied Sciences 41,
DOI 10.1007/978-3-319-27996-1_2

it might fail when computing solid or structural failure due to material failures. For this kind of problems, several modified arc-length methods were proposed, see e.g. [7, 15] and references therein. The problem of those modifications is that they are very much problem dependent. A general and robust path-following method for complete failure computation of solids and structures due to material failures is still to be designed.

The most important part of the path-following method is the constraint equation. Recently, [17] presented a path-following method based on constraint equation that is controlling dissipation of inelastic material. This kind of path-following method can be used when solid or structural material is modelled by an inelastic material model, e.g. by an elasto-plastic or damage model. In [17], several constraint functions were presented. In particular, they derived constraint functions for geometrically linear and geometrically nonlinear damage, and geometrically linear elasto-plasticity.

In this work we extent the ideas of [17] to geometrically nonlinear small strain elasto-plasticity and to embedded-discontinuity formulations. In particular, we derive explicit and implicit constraint functions that control incremental dissipation for small strain elasto-plasticity with isotropic hardening. Moreover, we derive explicit constraint functions, based on plastic dissipation control, for solid and beam embedded-strong-discontinuity-in-displacements (or rotation) finite elements. These kind of elements have become during the last years an interesting tool for modelling and simulation of solid or structural failure due to material failure, see e.g. [8, 12, 13]. Two of the authors of this work have been involved in derivation of the embedded-strong-discontinuity finite elements for analysis of different structures and solids. We refer to [2, 9, 14] for planar Euler-Bernoulli beams (Fig. 1), to [10] for Timoshenko beams (Fig. 2), and to [3, 4, 6] for 2d-solids (Fig. 3). In several cases, convergence problems were observed when computing failure analysis with those complex elements and standard cylindrical arc-length method. This problem is addressed in this work. The aim of this work is therefore a derivation of a novel path-following method, based on dissipation control, which should be more robust for analysis of solid and structural failure problems by the embedded-discontinuity finite elements.

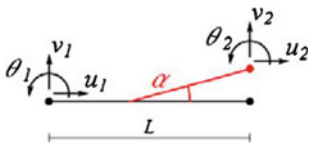

Fig. 1 Euler-Bernoulli beam finite element with embedded-strong-discontinuity in rotation. Cross-section softening in rotation is described by rigid-plasticity with softening

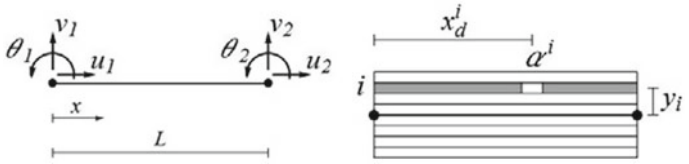

Fig. 2 Multi-layered Timoshenko beam finite element with layer-wise embedded-strong discontinuity in axial displacement. Material failure at each layer is described by rigid-plasticity with softening

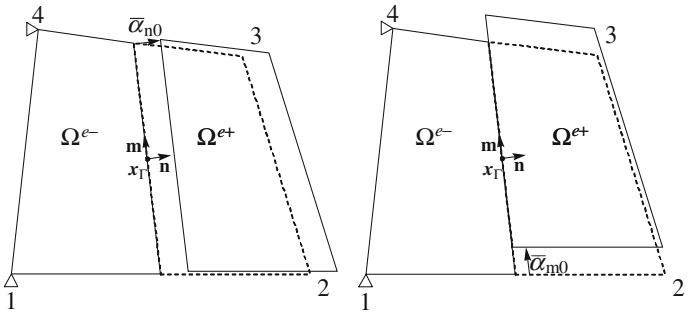

Fig. 3 2-d solid embedded-discontinuity quadrilateral: constant separations along the discontinuity line for mode I (*left*) and mode II (*right*). Cohesive stresses in discontinuity are described by rigid-plasticity with softening

2 Path-Following Method Framework

In the nonlinear finite element method for solids and structures, one has to solve a system of nonlinear equations related to the equilibrium of the nodes of the finite element mesh

$$\boldsymbol{R}\left(\boldsymbol{u}\left(t\right),\lambda\left(t\right)\right)=\boldsymbol{R}^{int}\left(\boldsymbol{u}\left(t\right)\right)-\boldsymbol{f}^{ext}\left(\lambda\left(t\right)\right)=\boldsymbol{0} \tag{1}$$

where $\boldsymbol{R}^{int}$ and $\boldsymbol{f}^{ext}$ are vectors of internal and external (equivalent) nodal forces (and moments, if they are present in the formulation), respectively, $\boldsymbol{u}$ is vector of unknown nodal displacements (and rotations, if they are present in the formulation), λ is the load convergence problems when factor, and $t \geq 0$ is a monotonically increasing parameter called the pseudo-time or the arc-length. In many practical cases, the system of Eq. (1) is possible to solve only by introducing an additional constraint equation

$$g\left(\boldsymbol{u}\left(t\right)-\boldsymbol{u}\left(t-\Delta t\right),\lambda\left(t\right)-\lambda\left(t-\Delta t\right)\right)=0 \tag{2}$$

where Δ is a (small) incremental change. Solving (1) and (2) simultaneously is called the path-following method or the arc-length method, see e.g. [1]. The solu-

tion of (1) and (2) is searched for at discrete pseudo-time points $0 = t_0, t_1, \ldots, t_n, t_{n+1}, \ldots, t_{final}$. Assume that configuration of solid or structure at t_n is known; it is defined by the pair $\{\boldsymbol{u}(t_n), \lambda(t_n)\} = \{\boldsymbol{u}_n, \lambda_n\}$. At searching for the next configuration at $t_{n+1} = t_n + \Delta t_n$, we decompose $\boldsymbol{u}_{n+1}$ and λ_{n+1} as

$$\boldsymbol{u}_{n+1} = \boldsymbol{u}_n + \Delta \boldsymbol{u}_n, \quad \lambda_{n+1} = \lambda_n + \Delta\lambda_n \tag{3}$$

where $\Delta \boldsymbol{u}_n$ and $\Delta\lambda_n$ are the increments of the displacement vector and the load vector, respectively. With (3), Eqs. (1) and (2) can be rewritten for t_{n+1} as

$$\begin{aligned} &\boldsymbol{R}_{n+1}(\boldsymbol{u}_n, \lambda_n; \Delta \boldsymbol{u}_n, \Delta\lambda_n) = \boldsymbol{0} \\ &g_{n+1}(\Delta \boldsymbol{u}_n, \Delta\lambda_n) = 0 \end{aligned} \tag{4}$$

where $\Delta \boldsymbol{u}_n$ and $\Delta\lambda_n$ are the unknowns. The solution of (4) is searched for iteratively by the Newton-Raphson method. At iteration i, the following linear system has to be solved

$$\begin{bmatrix} \boldsymbol{K}^i_{n+1} & \boldsymbol{R}^i_{n+1,\lambda} \\ \left[g^i_{n+1,\boldsymbol{u}}\right]^T & g^i_{n+1,\lambda} \end{bmatrix} \begin{Bmatrix} \Delta\tilde{\boldsymbol{u}}^i_n \\ \Delta\tilde{\lambda}^i_n \end{Bmatrix} = - \begin{Bmatrix} \boldsymbol{R}^i_{n+1} \\ g^i_{n+1} \end{Bmatrix} \tag{5}$$

for the pair $\left\{\Delta\tilde{\boldsymbol{u}}^i_n, \Delta\tilde{\lambda}^i_n\right\}$, where $(\circ)_{,\lambda}$ and $(\circ)_{,\boldsymbol{u}}$ denote the derivatives of $(\circ)$ with respect to $\Delta\lambda_n$ and $\Delta \boldsymbol{u}_n$, respectively, and $\boldsymbol{K}^i_{n+1} = \boldsymbol{R}^i_{n+1,\boldsymbol{u}}$ is the tangent stiffness matrix. New iterative guess is obtained as $\Delta \boldsymbol{u}^{i+1}_n = \Delta \boldsymbol{u}^i_n + \Delta\tilde{\boldsymbol{u}}^i_n$ and $\Delta\lambda^{i+1}_n = \Delta\lambda^i_n + \Delta\tilde{\lambda}^i_n$. System of Eq. (5) can be effectively solved by the bordering algorithm, see e.g. [18] for details. When the iteration loop ends due to fulfilment of a convergence criterion, the configuration $\{\boldsymbol{u}_{n+1}, \lambda_{n+1}\}$ at t_{n+1} is obtained and search for the solution at the next pseudo-time point can start.

The above presentation is valid for any kind of the constraint function g_{n+1} in (4). However, the robustness and efficiency of the path-following method depend crucially on the specific form of this function. In what follows, we will elaborate for the case when g_{n+1} controls the structural plastic dissipation, which can be computed when elasto-plastic and/or rigid-plastic material models are used.

3 Dissipation Constraint for Geometrically Nonlinear Small Strain Elasto-plasticity

In this section, we will present several formulations for defining constraint equation $g_{n+1} = 0$ in (4) that controls structural plastic dissipation.

3.1 Explicit Formulation—Version 1

The rate of plastic dissipation in an elasto-plastic solid or structure is defined as (see e.g. [8])

$$\dot{D} = \dot{P} - \dot{\Psi} \tag{6}$$

where $\dot{P}$ is the pseudo-time rate of the total energy the solid/structure is receiving, and $\dot{\Psi}$ is the rate of the thermodynamic (i.e. the free energy or the stored energy) potential for plasticity. For the discretized solid/structure in the framework of the geometrically nonlinear and inelastic finite element method, $\dot{P}$ can be written as

$$\dot{P} = \int_V \boldsymbol{S}^T \dot{\boldsymbol{E}} dV = \boldsymbol{f}^{ext,T} \dot{\boldsymbol{u}} = \lambda \hat{\boldsymbol{f}}^{ext,T} \dot{\boldsymbol{u}} \tag{7}$$

where $\boldsymbol{S}$ and $\boldsymbol{E}$ are vectors comprising 2nd Piola-Kirchhoff stresses and Green-Lagrange strains, respectively, and V is initial volume. Moreover, it was assumed in (1) and (7) that the external forces are conservative and can be described as $\boldsymbol{f}^{ext} = \lambda \hat{\boldsymbol{f}}^{ext}$, where $\hat{\boldsymbol{f}}^{ext}$ is a fixed pattern of nodal forces. The free energy potential (i.e. the stored energy) of a solid/structure, based on the St. Venant-Kirchhoff elasticity and plasticity with linear isotropic hardening, is

$$\Psi = U + H \tag{8}$$

where the stored energy due to elastic deformations is

$$U = \int_V \frac{1}{2} \boldsymbol{E}^{e,T} \boldsymbol{D} \boldsymbol{E}^e dV = \int_V \frac{1}{2} \boldsymbol{S}^T \boldsymbol{D}^{-1} \boldsymbol{S} dV \tag{9}$$

and the stored energy due to material hardening is

$$H = \int_V \frac{1}{2} K_h \xi_h^2 dV \tag{10}$$

Here, $\boldsymbol{E}^e = \boldsymbol{E} - \boldsymbol{E}^p$ are elastic strains, $\boldsymbol{E}^p$ are plastic strains, $\boldsymbol{D}$ is symmetric constitutive matrix, $\boldsymbol{S} = \boldsymbol{D}\boldsymbol{E}^e$, K_h is hardening modulus, and ξ_h is strain-like variable that controls isotropic hardening. For any other type of isotropic and/or kinematic hardening, H in (10) has to be changed accordingly. Derivation of U with respect to the pseudo-time gives

$$\dot{U} = \int_V \dot{\boldsymbol{E}}^T \boldsymbol{C}^{ep} \boldsymbol{D}^{-1} \boldsymbol{S} dV = \dot{\boldsymbol{u}}^T \int_V \boldsymbol{B}^T \boldsymbol{C}^{ep} \boldsymbol{D}^{-1} \boldsymbol{S} dV \tag{11}$$

where $\boldsymbol{C}^{ep}$ and $\boldsymbol{B}$ denote the consistent symmetric elasto-plastic tangent modulus and the strain-displacement matrix, respectively. The following relations were used in (11): $\dot{\boldsymbol{S}} = \boldsymbol{C}^{ep}\dot{\boldsymbol{E}}$, $\dot{\boldsymbol{E}} = \boldsymbol{B}\dot{\boldsymbol{u}}$. Derivation of H with respect to the pseudo-time yields

$$\dot{H} = \int_V K_h \xi_h \dot{\xi}_h dV = \int_V K_h \xi_h \left(\frac{\partial \xi_h}{\partial \boldsymbol{u}}\right)^T \dot{\boldsymbol{u}} \tag{12}$$

Let us use the forward Euler pseudo-time step to express dissipation at pseudo-time point t_{n+1} by using known dissipation at t_n

$$D_{n+1} = D_n + \dot{D}_n \Delta t_n, \quad \Delta t_n = t_{n+1} - t_n \tag{13}$$

Let us further define the following constraint equation

$$g_{n+1} = D_{n+1} - D_n - \tau_n = 0 \tag{14}$$

where τ_n is a predefined (required) value of dissipation at pseudo-time step $\left[t_n, t_{n+1}\right]$. It follows from (13), (6)–(8), (11) and (12) that (14) can be rewritten as

$$g_{n+1} = \dot{D}_n \Delta t_n - \tau_n = \Delta \boldsymbol{u}_n^T \left(\lambda_n \hat{\boldsymbol{f}}^{ext} - \boldsymbol{f}_n^*\right) - \tau_n = 0 \tag{15}$$

where $\Delta \boldsymbol{u}_n = \dot{\boldsymbol{u}}_n \Delta t_n$ was defined, and

$$\boldsymbol{f}_n^* = \int_V \boldsymbol{B}_n^T \boldsymbol{C}_n^{ep} \boldsymbol{D}^{-1} \boldsymbol{S}_n dV + \int_V K_h \xi_{h,n} \left(\frac{\partial \xi_h}{\partial \boldsymbol{u}}\right)_n dV \tag{16}$$

It follows from (15) that the derivatives needed in (5) are simply

$$g_{n+1,\lambda} = 0\,, \quad g_{n+1,\boldsymbol{u}} = \lambda_n \hat{\boldsymbol{f}}^{ext} - \boldsymbol{f}_n^* \tag{17}$$

Most of the terms in Eq. (16) are computed during the elasto-plastic analysis and can be readily used to compute (15) and (17). An exception is $(\partial \xi_h / \partial \boldsymbol{u})_n$. In practice, one should only compute $\boldsymbol{f}_n^*$ for configuration at t_n and use it in the path-following method when iterating to find configuration at t_{n+1}.

The second integral on the right hand side of (16) should be usually smaller than the first integral, which might be a justification for neglecting the former integral when computing (16), i.e.

$$\boldsymbol{f}_n^* \to \boldsymbol{f}_n^{*,approx} = \int_V \boldsymbol{B}_n^T \boldsymbol{C}_n^{ep} \boldsymbol{D}^{-1} \boldsymbol{S}_n dV \tag{18}$$

In such a case, the corresponding approximation $\left(\dot{D}_n \Delta t_n\right)^{approx}$ would be bigger than $\dot{D}_n \Delta t_n$ in (15).

3.2 Explicit Formulation—Version 2

An alternative for the expression (6) for the rate of plastic dissipation in an elasto-plastic solid or structure is (see e.g. [8])

$$\dot{D} = \int_V \left(\dot{\boldsymbol{E}}^{p,T} \boldsymbol{S} + \dot{\xi}_h q \right) dV \tag{19}$$

where $q = -K_h \xi_h$. Since $\dot{\boldsymbol{E}}^p = \dot{\boldsymbol{E}} - \dot{\boldsymbol{E}}^e = \left(\boldsymbol{I} - \boldsymbol{D}^{-1}\boldsymbol{C}^{ep}\right)\dot{\boldsymbol{E}}$, one can rewrite (19) as

$$\dot{D} = \int_V \dot{\boldsymbol{u}}^T \boldsymbol{B}^T \left(\boldsymbol{I} - \boldsymbol{D}^{-1}\boldsymbol{C}^{ep}\right)^T \boldsymbol{S} dV - \int_V \dot{\xi}_h K_h \xi_h dV \tag{20}$$

If (20) is used in (15), the constraint Eq. (15) transforms to

$$g_{n+1} = \dot{D}_n \Delta t_n - \tau_n = \Delta \boldsymbol{u}_n^T \bar{\boldsymbol{f}}_n - \tau_n = \boldsymbol{0} \tag{21}$$

where

$$\bar{\boldsymbol{f}}_n = \int_V \boldsymbol{B}_n^T \left(\boldsymbol{I} - \boldsymbol{D}^{-1}\boldsymbol{C}_n^{ep}\right)^T \boldsymbol{S}_n dV - \int_V K_h \xi_{h,n} \left(\frac{\partial \xi_h}{\partial \boldsymbol{u}}\right)_n dV \tag{22}$$

Comparison of (15) and (16) with (21) and (22) yields (note that $\left(\boldsymbol{I} - \boldsymbol{D}^{-1}\boldsymbol{C}_n^{ep}\right)^T = \boldsymbol{I} - \boldsymbol{C}_n^{ep}\boldsymbol{D}^{-1}$)

$$\lambda_n \hat{\boldsymbol{f}}^{ext} = \int_V \boldsymbol{B}_n^T \boldsymbol{S}_n dV \tag{23}$$

which states that the equivalent external nodal forces are in equilibrium with the internal nodal forces at t_n, see e.g. [8], a condition already accomplished at the start of the current pseudo-time step $\left[t_n, t_{n+1}\right]$. This leads us to a conclusion that constraints (15) and (21) are completely equivalent but computed differently. The derivatives of (21) are

$$g_{n+1,\lambda} = 0\,, \quad g_{n+1,\boldsymbol{u}} = \bar{\boldsymbol{f}}_n \tag{24}$$

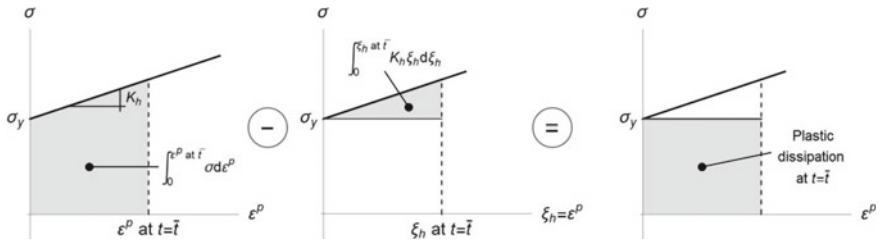

Fig. 4 Plastic dissipation at bulk point of elasto-plastic material with hardening for pseudo-time increment $[t_y, \bar{t}]$ and 1d case

It can be seen from (19) and (22) that approximation (18) corresponds to approximation

$$\dot{D} \to \dot{D}^{approx} = \int_V \dot{\boldsymbol{E}}^{p,T} \boldsymbol{S} dV \tag{25}$$

For a 1d case, i.e. stretching/compressing of a bar, integration of (25) relates to Fig. 4 (left), and integration of (19) and (20) relates to Fig. 4 (right). In Fig. 4, plastic yielding at a material point of such a bar is presented, where σ, ε^p, and σ_y denote stress, plastic strain and yield stress, respectively. Let us look at the plastic dissipation at the end of the pseudo-time increment $[t_y, \bar{t}]$, where t_y is the pseudo-time point at the beginning of plastic yielding. Since the stress monotonically increases during this increment, $\varepsilon^p = \xi_h$, see [8]. Plastic dissipation at a material point at $t = \bar{t}$ is the grey area on Fig. 4 (right). When energy storage in the material point due to material hardening is neglected, an approximation of plastic dissipation at $t = \bar{t}$ is obtained, which is bigger than the plastic dissipation and corresponds to the grey area on Fig. 4 (left).

Equation that corresponds to (18) and (25), i.e. (15) without the "hardening term" (more precisely, (15) without the second integral on the right hand side of Eq. (16)), was used in [17] for geometrically linear elasto-plastic problems. However, it is clear from the above derivations that the constraints (15) and (21) can be both used for geometrically linear as well as for geometrically nonlinear small-strain elasto-plastic problems.

3.3 Implicit Formulations

In this section, we present implicit counterparts of version-1 and version-2 explicit formulations presented above. The backward Euler pseudo-time step can be used in (13), i.e.

$$D_{n+1} = D_n + \dot{D}_{n+1}\Delta t_n, \quad \Delta t_n = t_{n+1} - t_n \tag{26}$$

which leads to the following constraint equation (compare with (15))

$$g_{n+1} = \dot{D}_{n+1}\Delta t_n - \tau_n = \Delta \boldsymbol{u}_n^T \left(\lambda_{n+1}\hat{\boldsymbol{f}}^{ext} - \boldsymbol{f}^*_{n+1}\right) - \tau_n = 0 \tag{27}$$

where

$$\boldsymbol{f}^*_{n+1} = \int_V \boldsymbol{B}^T_{n+1}\boldsymbol{C}^{ep}_{n+1}\boldsymbol{D}^{-1}\boldsymbol{S}_{n+1}dV + \int_V K_h\xi_{h,n+1}\left(\frac{\partial \xi_h}{\partial \boldsymbol{u}}\right)_{n+1} dV \tag{28}$$

Note that $\Delta \boldsymbol{u}_n$ in (27) is defined as $\Delta \boldsymbol{u}_n = \dot{\boldsymbol{u}}_{n+1}\Delta t_n$. Expressions for the derivatives of g_{n+1} are much more complex in comparison with (17) and can be written as

$$g_{n+1,\lambda} = \Delta \boldsymbol{u}_n^T \hat{\boldsymbol{f}}^{ext}, \quad g_{n+1,\boldsymbol{u}} = \lambda_{n+1}\hat{\boldsymbol{f}}^{ext} - \boldsymbol{f}^*_{n+1} - \left(\boldsymbol{f}^*_{n+1,\boldsymbol{u}}\right)^T \Delta \boldsymbol{u}_n \tag{29}$$

The problem is to derive $\boldsymbol{f}^*_{n+1,\boldsymbol{u}}$, which demands, among other derivatives, the derivative of elasto-plastic tangent modulus $\boldsymbol{C}^{ep}_{n+1,\boldsymbol{u}}$.

Alternatively to (27), the constraint equation can be expressed as (compare with (21))

$$g_{n+1} = \dot{D}_{n+1}\Delta t_n - \tau_n = \Delta \boldsymbol{u}_n^T \bar{\boldsymbol{f}}_{n+1} - \tau_n = 0 \tag{30}$$

where

$$\bar{\boldsymbol{f}}_{n+1} = \int_V \boldsymbol{B}^T_{n+1}\left(\boldsymbol{I} - \boldsymbol{D}^{-1}\boldsymbol{C}^{ep}_{n+1}\right)^T \boldsymbol{S}_{n+1}dV - \int_V K_h\xi_{h,n+1}\left(\frac{\partial \xi_h}{\partial \boldsymbol{u}}\right)_{n+1} dV \tag{31}$$

and

$$g_{n+1,\lambda} = 0, \quad g_{n+1,\boldsymbol{u}} = \bar{\boldsymbol{f}}_{n+1} - \left(\bar{\boldsymbol{f}}_{n+1,\boldsymbol{u}}\right)^T \Delta \boldsymbol{u}_n \tag{32}$$

where, again, $\bar{\boldsymbol{f}}_{n+1,\boldsymbol{u}}$ calls for derivative of elasto-plastic tangent modulus $\boldsymbol{C}^{ep}_{n+1,\boldsymbol{u}}$.

It is obvious that $\boldsymbol{f}^*_{n+1,\boldsymbol{u}}$ and $\bar{\boldsymbol{f}}_{n+1,\boldsymbol{u}}$, needed in (29) and (32), respectively, are not easy to derive and compute, which renders explicit formulations more attractive for implementation than implicit. On the other hand, the explicit formulations might turn to be less robust than the implicit ones.

4 Dissipation Constraint for Embedded Discontinuity Finite Elements

Let us derive the plastic dissipation constraint for a situation when the material failure in solid is modelled by the embedded-displacement-discontinuity finite element formulation and inelastic softening cohesive traction-separation law is used at the

discontinuity. In what follows, we will restrict to 2-d solids with a single fracture curve (i.e. with a single discontinuity) and to frames with softening plastic hinges. Let the bulk of the 2-d solid or frame be modelled as elastic and let the cohesive stresses at the discontinuity be modelled by rigid-plasticity with linear softening.

The free energy potential (i.e. the stored energy) of the solid can be written as

$$\Psi = (U - S) + S_s \tag{33}$$

where the stored energy due to elastic deformations of the bulk

$$U = \int_V \frac{1}{2} \boldsymbol{E}^T \boldsymbol{D} \boldsymbol{E} dV = \int_V \frac{1}{2} \boldsymbol{S}^T \boldsymbol{D}^{-1} \boldsymbol{S} dV \tag{34}$$

is diminished for S due to localized plastic deformations at the failure curve. Due to softening rigid-plasticity, those plastic deformations equal to kinematic variables $\boldsymbol{\alpha}$ that describe material separation along the discontinuity. The S in (33) is defined as

$$S = \int_\Gamma \boldsymbol{\alpha}^T \boldsymbol{t} d\Gamma \tag{35}$$

where $\boldsymbol{t}$ is vector of cohesive stresses in discontinuity, and Γ is length of the discontinuity curve. The S_s in (33) is due to the linear softening and takes the form

$$S_s = \int_\Gamma \frac{1}{2} K_s \xi_s^2 d\Gamma \tag{36}$$

In (36), $K_s < 0$ is softening modulus, and ξ_s is displacement-like variable that controls softening. The pseudo-time derivatives of (34), (35) and (36) are

$$\dot{U} = \int_V \dot{\boldsymbol{E}}^T \boldsymbol{S} dV, \quad \dot{S} = \int_\Gamma \dot{\boldsymbol{\alpha}}^T \boldsymbol{t} d\Gamma, \quad \dot{S}_s = \int_\Gamma K_s \xi_s \dot{\xi}_s d\Gamma \tag{37}$$

The derivatives in (37) can be expressed by $\dot{\boldsymbol{u}}$ using $\dot{\boldsymbol{E}} = \boldsymbol{B}\dot{\boldsymbol{u}}$ and the chain rule

$$\dot{\boldsymbol{\alpha}} = \frac{\partial \boldsymbol{\alpha}}{\partial \boldsymbol{u}} \dot{\boldsymbol{u}}, \quad \dot{\xi}_s = \left(\frac{\partial \xi_s}{\partial \boldsymbol{\alpha}} \right)^T \frac{\partial \boldsymbol{\alpha}}{\partial \boldsymbol{u}} \dot{\boldsymbol{u}} \tag{38}$$

The constraint equation can be defined for forward Euler pseudo-time step (according to the version-1 of above presented explicit formulation, see (15)) as

$$g_{n+1} = \dot{D}_n \Delta t_n - \tau_n = \Delta \boldsymbol{u}_n^T \left(\lambda_n \hat{\boldsymbol{f}}^{ext} - \boldsymbol{f}_n^* \right) - \tau_n = 0 \tag{39}$$

where $\boldsymbol{f}_n^*$ in (39) is now defined as

$$\boldsymbol{f}_n^* = \int_V \boldsymbol{B}_n^T \boldsymbol{S}_n dV + \underbrace{\int_\Gamma \left(\frac{\partial \boldsymbol{\alpha}}{\partial \boldsymbol{u}}\right)_n^T \boldsymbol{t}_n d\Gamma + \int_\Gamma K_s \xi_{s,n} \left(\frac{\partial \boldsymbol{\alpha}}{\partial \boldsymbol{u}}\right)_n^T \left(\frac{\partial \xi_s}{\partial \boldsymbol{\alpha}}\right)_n d\Gamma}_{\bar{\boldsymbol{f}}_n^*} \tag{40}$$

The equilibrium of solid or structure at t_n demands equality of external and internal nodal forces, i.e. $\lambda_n \hat{\boldsymbol{f}}^{ext} = \int_V \boldsymbol{B}_n^T \boldsymbol{S}_n dV$. Thus, inserting (40) in (39) yields

$$g_{n+1} = \dot{D}_n \Delta t_n - \tau_n = \Delta \boldsymbol{u}_n^T \bar{\boldsymbol{f}}_n^* - \tau_n = 0 \tag{41}$$

where $\bar{\boldsymbol{f}}_n^*$ is indicated in (40). The derivatives of g_{n+1} are the expressions from (17) with $\boldsymbol{f}_n^*$ from (40). In the implementation of embedded-discontinuity finite elements, kinematic variables $\boldsymbol{\alpha}$ are condensed on the element level. This enables to compute $(\partial \boldsymbol{\alpha}/\partial \boldsymbol{u})_n$ in (40) as assembly of element contributions. Since the condensation on the element level (e) yields

$$\Delta \boldsymbol{\alpha}_n^{(e)} = \left(\boldsymbol{K}^{\boldsymbol{\alpha\alpha},(e)}\right)_n^{-1} \boldsymbol{K}_n^{\boldsymbol{\alpha u},(e)} \Delta \boldsymbol{u}_n^{(e)}, \quad \boldsymbol{K}_n^{(e)} = \begin{bmatrix} \boldsymbol{K}^{\boldsymbol{uu}} & \boldsymbol{K}^{\boldsymbol{u\alpha}} \\ \boldsymbol{K}^{\boldsymbol{\alpha u}} & \boldsymbol{K}^{\boldsymbol{\alpha\alpha}} \end{bmatrix}_n^{(e)} \tag{42}$$

one has

$$\left(\frac{\partial \boldsymbol{\alpha}}{\partial \boldsymbol{u}}\right)_n^{(e)} = \left(\boldsymbol{K}^{\boldsymbol{\alpha\alpha},(e)}\right)_n^{-1} \boldsymbol{K}_n^{\boldsymbol{\alpha u},(e)} \tag{43}$$

where $\boldsymbol{K}_n^{(e)}$ is the element stiffness matrix at t_n, which can be decomposed as shown in (42). How $(\partial \xi_s/\partial \boldsymbol{u})_n$ in (40) is computed will not be further elaborated.

The third integral on the right hand side of (40) might be neglected, i.e.

$$\bar{\boldsymbol{f}}_n^* \to \bar{\boldsymbol{f}}_n^{*,approx} = \int_\Gamma \left(\frac{\partial \boldsymbol{\alpha}}{\partial \boldsymbol{u}}\right)_n^T \boldsymbol{t}_n d\Gamma \tag{44}$$

The corresponding approximation $\left(\dot{D}_n \Delta t_n\right)^{approx}$ is smaller than $\dot{D}_n \Delta t_n$ in (41) since $K_s < 0$. This is illustrated for 1d case, i.e. stretching/compressing of a bar, in Fig. 5, where plastic dissipation for a point at the discontinuity is presented. For a 1d case integration of (41) relates to Fig. 5 (right), and integration of (41) by using (44) relates to Fig. 5 (left). In Fig. 5, f is cohesive stress, f_f is material failure stress at which

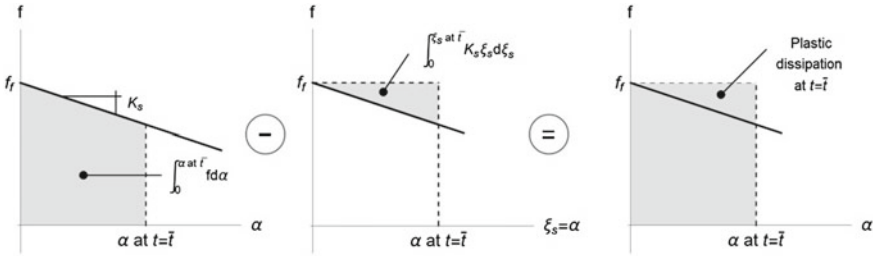

Fig. 5 Plastic dissipation at discontinuity point for rigid-plastic material with linear softening for pseudo-time increment $[t_y, \bar{t}]$ and 1d case

softening begins, and α is separation. The plastic dissipation at the end of the pseudo-time increment $[t_f, \bar{t}]$ is shown, where t_f is pseudo-time point at material failure. Since the cohesive stress monotonically decreases during this increment, $\alpha = \xi_s$. Plastic dissipation at a material point at $t = \bar{t}$ is the grey area on Fig. 5 (right). When material softening is neglected, an approximation of plastic dissipation at $t = \bar{t}$ is obtained, which is smaller than the plastic dissipation and corresponds to the grey area on Fig. 5 (left).

The above derivation is the embedded-discontinuity softening-rigid-plasticity counterpart of the concepts introduced above in section "Explicit formulation—version 1". If one wants to exploit the concepts from "Explicit formulation—version 2", the rate of plastic dissipation has to be considered, which is defined as (since the plastic dissipation takes place only at the discontinuity curve)

$$\dot{D} = \int_{\Gamma} \left(\dot{\boldsymbol{\alpha}}^T \boldsymbol{t} + \dot{\xi}_s q_s \right) d\Gamma \tag{45}$$

where $q_s = -K_s \xi_s$. It is straightforward to show that the constraint equations related to (45) is (41). The corresponding implicit formulation will not be considered here.

When dealing with frames with elastic bulk and softening plastic hinges, the integral over the discontinuity curve in the expressions above is replaced with the sum over discontinuity points (i.e. the sum over softening plastic hinges). For example, in such a case, (35) transforms to

$$S = \sum_{i=1}^{n_p} \boldsymbol{\alpha}_i^T \boldsymbol{t}_i \tag{46}$$

where n_p is number of discontinuity points in the frame, and $\boldsymbol{\alpha}_i$ and $\boldsymbol{t}_i$ are vectors comprising jumps in displacements and rotations and cohesive forces and moments, respectively at i-th softening plastic hinge.

5 Numerical Examples

In this section, we present two examples. The following finite elements are used: (i) 4-node assumed natural strain (ANS) shell element with stress-resultant Ilyushin-Shapiro elasto-plasticity (which is a shell stress-resultant counterpart of shell J_2 plasticity with hardening and von Mises yield criterion), see [5], (ii) stress-resultant planar Euler-Bernoulli beam element with embedded-discontinuity in rotation representing softening plastic hinge. The used material models are elasto-plasticity with hardening (for the bulk) and rigid-plasticity with softening (for the discontinuity point), see Fig. 1 and [2, 9]. Those elements and plastic dissipation based path-following method have been implemented into the computer code AceFEM, see [11]

The path-following method that is used for the analysis of the first example is based on Eq. (15) with $\boldsymbol{f}_n^*$ computed with (18). For the initial, i.e. elastic, part of the response, standard cylindrical Crisfield arc-length method was used, see e.g. [1], with

$$g_{n+1} = \Delta \boldsymbol{u}_n^T \Delta \boldsymbol{u}_n - \tau_n \tag{47}$$

see also [16]. The path-following method that is used for the analysis of the second example is based on the sum of two above presented equations: (i) equation (15) that takes into account plastic dissipation due to hardening plasticity ($\boldsymbol{f}_n^*$ in (15) was computed with (18)), and (ii) Eq. (41) that takes into account plastic dissipation due to softening ($\bar{\boldsymbol{f}}_n^*$ in (41) was computed with (44) and (46)).

5.1 Geometrically Nonlinear Elasto-plastic Shell Analysis

We consider cylindrical panel from Fig. 6, which is subjected to a set of horizontal axial forces λH_0 (where $H_0 = 1000\,\mathrm{N}$), applied at each node of the mesh at curved edge at $y = 0$, and to a vertical point load λV_0 (where $V_0 = 10\,\mathrm{N}$). Geometry and boundary conditions of the panel with thickness h are presented in Fig. 6. The panel is made of isotropic elasto-plastic material (steel) with elastic modulus $E = 210{,}000\,\mathrm{N/mm^2}$, Poisson's coefficient $\nu = 0.3$, yield stress $\sigma_y = 235\,\mathrm{N/mm^2}$ and hardening modulus $K_h = 0$. Finite element mesh consists of 24×24 elements. Table 1 presents the input data for used path-following methods. The analysis started with standard arc-length, which was later replaced with the dissipation controlled path-following method.

Figure 7 shows initial and deformed finite element meshes. Load factor λ versus vertical displacement curves for the two nodes, marked on Fig. 7 (left), are presented in Fig. 8. At point A on Fig. 8, the Crisfield cylindrical arc-length, see (47) and Table 1, failed to converge. If the solution method was switched to the dissipation

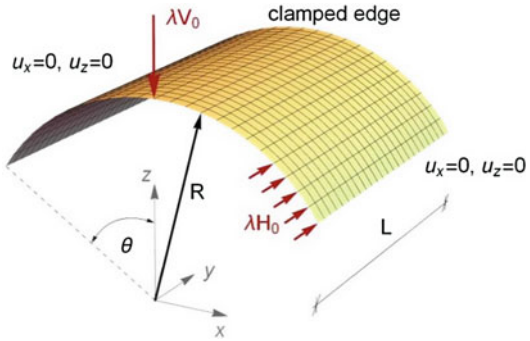

$R = 1270$ mm
$L = 2032$ mm
$\theta = 57.30°$
$h = 5$ mm

Fig. 6 Shell panel data

Table 1 Elasto-plastic shell: data for used path-following methods

	τ_0	$\tau_{n,max}$	Desired number of iterations	Convergence tolerance
Arc-length	0.5	1	8	10^{-8}
Dissipation based	10^2 Nmm	10^5 Nmm	8	10^{-8}

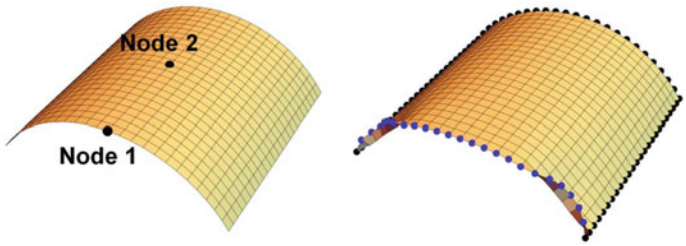

Fig. 7 Initial mesh and deformed mesh (at the end of the analysis, see Fig. 8)

based path-following method after the plasticity had started (which was before point A), the solution path could be traced much beyond point A. This example illustrates that the dissipation based path-following method may be superior to the cylindrical arc-length for elasto-plastic problems.

5.2 *Failure of Steel Frame*

A planar steel frame from Fig. 9 is analysed with the stress-resultant elasto-plastic geometrically linear beam Euler-Bernoulli finite element with the embedded strong

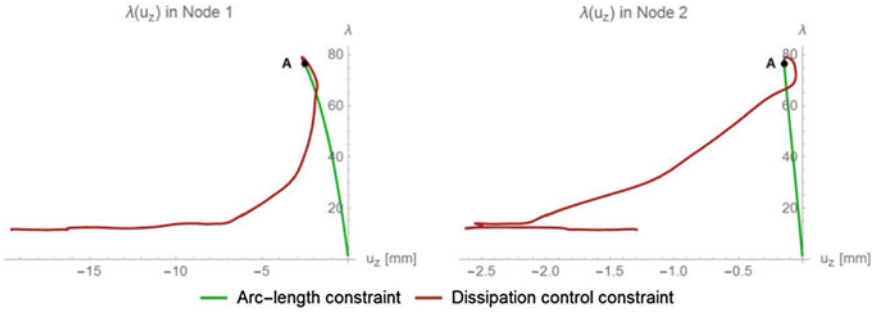

Fig. 8 Load factor versus vertical displacement u_z for nodes 1 and 2

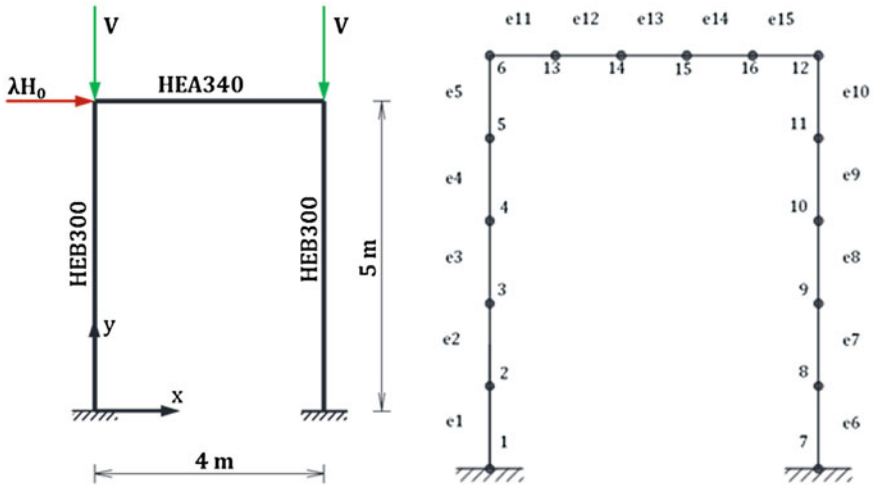

Fig. 9 Planar steel frame and the finite element mesh

discontinuity in rotation, see e.g. [2] and Fig. 1. The columns and the beam are discretized as shown on Fig. 9 (right). The material Young's modulus is $E = 210{,}000\,\mathrm{N/mm^2}$ and the yield stress is $\boldsymbol{\sigma}_y = 235\,\mathrm{N/mm^2}$. It is assumed that the yield moment of a cross-section depends on the axial force N as

$$M_y(N) = W\left(\sigma_y - \frac{|N|}{A}\right) \tag{48}$$

where W is the bending resistance cross-section modulus, and A is the cross-section area. Moreover, it is assumed that the ultimate moment M_u is also a function of the axial force N as

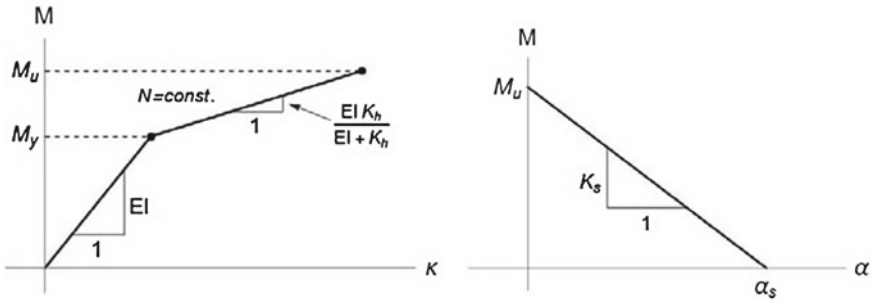

Fig. 10 Moment-curvature relation for the integration point. Moment versus jump in rotation line for the plastic hinge

$$M_u(N) = \begin{cases} M_u^{ref,0}\left(1.03 + 0.85\frac{N}{N_y}\right) & if \quad N < -0.035N_y \\ M_u^{ref,0} & if \quad N \geq -0.035N_y \end{cases} \tag{49}$$

where $N_y = A\sigma_y$ and $M_u^{ref,0} = W_{pl}\sigma_y$, where W_{pl} is the plastic modulus. The stress-resultant elasto-plasticity for the bulk is presented in Fig. 10 (left). The rigid-plasticity with softening, used in rotational softening plastic hinge, is presented in Fig. 10 (right). It is assumed that softening rotational hinge response is governed by linear softening modulus K_s.

The data for the HEA340 are: $A = 12721.5\,\text{mm}^2$, modulus of inertia $I = 264{,}213{,}316\,\text{mm}^4$, $W_{pl} = 1{,}761{,}321\,\text{mm}^3$, linear hardening modulus $K_h = 5.3{\cdot}10^{11}\,\text{Nmm}^2$, $K_s = -2.0{\cdot}10^9\,\text{Nmm}$. The data for the HEB300 are: $A = 14{,}282\,\text{mm}^2$, $I = 241{,}867{,}801\,\text{mm}^4$, $W_{pl} = 1{,}780{,}471\,\text{mm}^3$, $K_h = 6.3{\cdot}10^{11}\,\text{Nmm}^2$ and $K_s = -2.0{\cdot}10^9\,\text{Nmm}$. The load consists of the horizontal force λH_0, where $H_0 = 35\,\text{kN}$ and two vertical forces $V = 2800\,\text{kN}$ that remain constant throughout the analysis.

The standard arc-length method (see Table 2) failed to converge at point A on Fig. 11. If we replaced it by the path-following method with dissipation control (see Table 2) after the activation of the first plastic hinge, complete failure was computed. Figure 12 (left) shows deformed configuration at point B marked on Fig. 11. The value of plastic rotation at softening plastic hinges at that configuration are presented in Fig. 12 (right).

Table 2 Planar steel frame: data for used path-following methods

	τ_0	$\tau_{n,max}$	Desired number of iterations	Convergence tolerance
Arc-length	500	500	5	10^{-10}
Dissipation based	1 Nmm	10^5 Nmm	5	10^{-10}

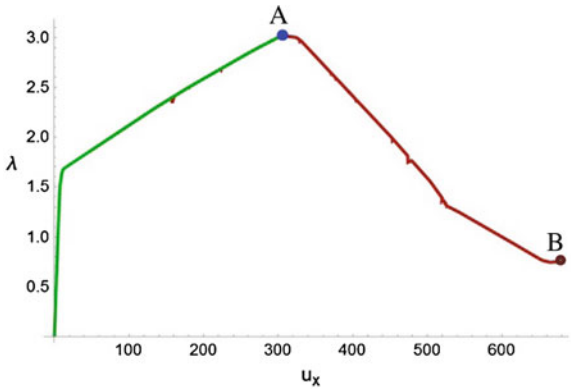

Fig. 11 Load factor versus horizontal displacement of the upper left corner of the frame

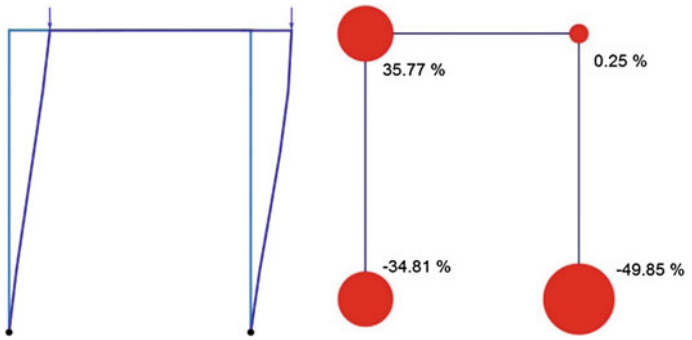

Fig. 12 Deformed configuration. Plastic hinges and corresponding ratio of plastic rotation α/α_s (in percentage)

6 Conclusions

In the first part of this work, we studied in detail different constraint functions for controlling incremental plastic dissipation in geometrically nonlinear elasto-plastic solid and structural problems. The derived constraint functions can be used to govern a dissipation-based path-following method for elasto-plasticity with isotropic hardening, which is an extension of the work presented in [17]. It turned out (see 1st example in "Numerical examples") that the resulting path-following method can be superior to the standard cylindrical Crisfiled's arc-length method [1]. Moreover, one should have in mind that the latter method sometimes allows for unrealistic, spurious elastic unloading of a complete structure [15]. This cannot happen with the dissipation-based path-following method, since elastic unloading of complete structure is not possible when using this method.

In the second part of the work, the dissipation-based path-following method was extended to embedded-discontinuity finite element formulations. Those formulations

are used to model material failure in solids and structures. The constraint functions were derived for 2d-solid and plane-frame embedded-discontinuity finite elements that represent cohesive stresses (or forces and moments) in the discontinuity by rigid-plasticity with softening. It turned out that the dissipation-based path-following method is very suitable for computation of complete failure of solids and structures by using embedded-discontinuity finite elements (see 2nd example in "Numerical examples"). It should be also very robust for any other finite element formulation involving material softening.

References

1. Crisfield, M.A. 1991. Non-linear Finite Element Analysis of Solids and Structures, Vol. 1: Essentials, Chichester. John Wiley & Sons: 345 p.
2. Dujc, J., Brank, B., Ibrahimbegovic, A. 2010. Multi-scale computational model for failure analysis of metal frames that includes softening and local buckling. The fractional Fourier transform and applications. Computer Methods in Applied Mechanics and Engineering, 199: 1371–1385.
3. Dujc, J., Brank, B., Ibrahimbegovic, A., Brancherie, D. 2010. An embedded crack model for failure analysis of concrete solids. Computers and Concrete, 7 (4): 331–346.
4. Dujc, J., Brank, B., Ibrahimbegovic, A. 2010. Quadrilateral finite element with embedded strong discontinuity for failure analysis of solids. CMES - Computer Modeling in Engineering and Sciences, 69 (3): 223–258.
5. Dujc, J., Brank, B. 2012. Stress resultant plasticity for shells revisited. Computer Methods in Applied Mechanics and Engineering, 247–248: 146–165.
6. Dujc, J., Brank, B., Ibrahimbegovic, A. 2013. Stress-hybrid quadrilateral finite element with embedded strong discontinuity for failure analysis of plane stress solids. International Journal for Numerical Methods in Engineering, 94 (12): 1075–1098.
7. Geers, M.G.D. 1999. Enhanced solution control for physically and geometrically non-linear problems. Part I - The subplane control approach. International Journal for Numerical Methods in Engineering, 46 (2): 177–204.
8. A. Ibrahimbegovic. 2009. Nonlinear solid mechanics. Theoretical formulations and finite element solution methods. Springer: 594 p.
9. Jukić, M., Brank, B., Ibrahimbegović, A. 2013. Embedded discontinuity finite element formulation for failure analysis of planar reinforced concrete beams and frames. Engineering Structures, 50: 115–125.
10. Jukić, M., Brank, B., Ibrahimbegovic, A. 2014. Failure analysis of reinforced concrete frames by beam finite element that combines damage, plasticity and embedded discontinuity. Engineering Structures, 75: 507–527.
11. Korelc, J. 2015. AceGen and AceFEM. Available at http://www.fgg.uni-lj.si/Symech
12. Linder, C., Armero, F. 2007. Finite elements with embedded strong discontinuities for the modeling of failure in solids. International Journal for Numerical Methods in Engineering, 72 (12), pp. 1391–1433.
13. Oliver, J., Huespe, A.E. 2004. Theoretical and computational issues in modelling material failure in strong discontinuity scenarios. Computer Methods in Applied Mechanics and Engineering, 193 (27–29): 2987–3014.
14. Piculin, S., Brank, B. 2015. Weak coupling of shell and beam computational models for failure analysis of steel frames. Finite Elements in Analysis and Design, 97: 20–42.
15. Pohl, T., Ramm, E., Bischoff, M. 2014. Adaptive path following schemes for problems with softening. Finite Elements in Analysis and Design, 86: 12–22.

16. Stanić, A., Brank, B., Korelc, J. 2015. On consistently linearized path-following method and its application to structural failure problems. Submitted for publication.
17. Verhoosel, C.V., Remmers, J.J.C., Gutiérrez, M.A. 2009. A dissipation-based arc-length method for robust simulation of brittle and ductile failure. International Journal for Numerical Methods in Engineering, 77 (9): 1290–1321.
18. Wriggers, P. 2008. Nonlinear Finite Element Methods. Springer.

Springer

http://www.springer.com/978-3-319-27994-7

Computational Methods for Solids and Fluids
Multiscale Analysis, Probability Aspects and Model Reduction

Ibrahimbegovic, A. (Ed.)
2016, XII, 493 p. 224 illus. in color., Hardcover
ISBN: 978-3-319-27994-7